

Research Paper

Non-differential water vapor estimation from SBAS-InSAR



Meng Duan, Bing Xu ^{*}, Zhiwei Li ^{**}, Yunmeng Cao, Jun Hu, Wenbin Xu, Jianchao Wei, Guangcai Feng

School of Geosciences and Info-Physics, Central South University, Changsha, 410083, Hunan, China

ARTICLE INFO

Keywords:
Interferometric synthetic aperture radar
Rank deficiency
Precipitable water vapor
Constraint condition
Time series

ABSTRACT

Water vapor is the most variable constituent in the atmosphere and plays an important role in climate studies, mesoscale meteorology modeling and numerical weather forecasting. Being able to penetrate clouds, interferometric synthetic aperture radar (InSAR) shows great potential in atmospheric water vapor mapping. But InSAR can only measure differential water vapor between two acquisitions. In this paper, we formulate a general framework by constructing the Gauss-Markov model and developing the estimation method to retrieve the non-differential water vapor from Small Baseline Subset InSAR (SBAS-InSAR). To address the rank-deficiency in the Gauss-Markov model, we propose a new constraint, i.e., the temporal mean of water vapor being invariant. Simulated and real data experiments are conducted to validate the effectiveness of the framework and the advantages of the proposed constraint. The results show that the new constraint can offer an estimation more robust than the two traditional ones, i.e., the temporal mean of water vapor being zero and single or multiple epoch water vapor referencing. In addition, we found that there exists a constant bias, which equals to the temporal mean of water vapors, between the solutions under the new constraint and that under the constraint of the temporal mean of water vapor being zero. Finally, the possible methods to evaluate the temporal mean of water vapor are discussed.

1. Introduction

Water vapor is the most variable constituent in the atmosphere. It influences the Earth's radiation budget, energy transfer, cloud formation and precipitation (Duan et al., 1996; Philipona et al., 2005; Zhao et al., 2016), and plays a key role in climate study, mesoscale meteorology modeling and numerical weather forecasting (Bevis et al., 1992; Yan et al., 2009). Over the past decades, many techniques have been proposed to measure the water vapor, e.g., Radiosondes, water vapor radiometer, Global Navigation Satellite System (GNSS), and imaging spectroradiometer. However, Radiosondes (Li et al., 2003; Zhang et al., 2018) or water vapor radiometer measurements (Niell et al., 2001) have limited spatial and temporal resolutions. GNSS measurements can provide PWV with a dense temporal sampling. However, their spatial resolution is always not high enough to capture the variations of the local water vapor (Benevides et al., 2016). The passive multispectral imager, such as Moderate Resolution Imaging Spectroradiometer (MODIS) and Medium Resolution Imaging Spectrometer (MERIS), can only measure water vapor in the daytime under cloud-free conditions (Li, 2005;

Bennartz and Fischer, 2001). Besides, the spatial resolution of the measurements is poor. These limitations degrade the quality of short-term (0–24 h) precipitation prediction.

Interferometric synthetic aperture radar (InSAR) is a powerful earth observation technology, with all-weather and day-and-night imaging capability, wide spatial coverage, fine resolution and competitive accuracy (Massonnet and Feigl, 1998). Atmospheric delay in InSAR is dominated by water vapor and can be estimated pixel by pixel. This offers a great potential to derive high spatial resolution water vapor from InSAR observations by analyzing the InSAR atmospheric delay. However, as a relative measurement tool, InSAR can only estimate the differential water vapor between two SAR acquisitions (Hanssen et al., 1999; Li et al., 2006). Many studies have demonstrated the ability of InSAR in estimating high-resolution differential precipitable water vapor (PWV) (Matus et al., 2011, 2018; Benevides et al., 2016; Chang et al., 2016; Tang et al., 2016), but how to estimate the non-differential PWV from InSAR have not been systematically investigated and satisfactorily resolved. Until now, only several studies applied InSAR to estimate non-differential PWV. Liu (2012) proposed to evaluate the

^{*} Corresponding author. School of Geosciences and Info-Physics, Central South University, Changsha, Hunan, China.

^{**} Corresponding author. Department of Geomatics, School of Geosciences and Info-Physics, Central South University, Changsha, Hunan, China.

E-mail addresses: xubing@csu.edu.cn (B. Xu), zwli@csu.edu.cn (Z. Li).

non-differential PWV of the master SAR image by the Least-Squares Collocation (LSC) in time domain firstly, and then used the LSC algorithm to estimate the non-differential PWV of each slave image in space domain. However, this approach is only suitable to the interferograms with a common master image. Meanwhile, it is based on the assumptions that water vapor in troposphere is isotropic and spatially stationary. Similarly, Pichelli et al. (2015) first estimated the master image's PWV by introducing a constraint (i.e., the external PWV from Medium Resolution Imaging Spectrometer), and then evaluated the PWVs corresponding to each slave SAR image of the generated interferograms. But it is unsuitable to the multiple master images' case. However, errors in the master image would be passed to slave images by interferograms in terms of the theory of error transfer and the larger the time interval between the master and slave image, the lower the estimation accuracy. In addition, this method is not applicable to the case of multiple master image interferograms. Another way to add constraint is assuming the temporal mean of water vapor being zero (Alshawaf et al., 2015). This method, however, needs a large number of SAR images and is only applicable to flat region. Additionally, if one of the SAR images was obtained under extreme weather such as thunderstorms, the PWVs derived from this method would be contaminated greatly.

To overcome these limitations, we formulate a general framework to estimate the non-differential water vapor based on SBAS-InSAR, and develop a new constraint, the temporal mean of water vapor being invariant, to stabilize the system of water vapor estimation under the framework. The rest of this paper is organized as follows. Section 2 constructs the Gauss-Markov model for non-differential water vapor estimation from SBAS-InSAR, and Section 3 schematically discusses the non-differential water vapor estimation based on the Gauss-Markov model and traditional constraints. In Section 4, we propose a new constraint, followed by the experiments using the simulation and real data in Section 5. Discussions are presented in Section 6 to address the influences of constraints on non-differential water vapor estimation and the possible determinations of temporal mean of water vapor. Finally, some conclusions are drawn in Section 7.

2. Gauss-Markov model for non-differential water vapor estimation from SBAS-InSAR

Give N SAR images and each image with $r \times c$ pixels (r and c represent the number of rank and column, respectively) was acquired from the same satellite track at time epochs (t_1, \dots, t_N) . We assume that these images are coregistered to a common reference geometry. A network with M (where $N/2 \leq M \leq N(N - 1)/2$) interferometric pairs is constructed with the N coregistered SAR images. Each interferometric pair is processed according to the standard differential InSAR and all differential interferograms are correctly unwrapped. Assume that η pixels are selected to estimate the non-differential water vapor in time series. The unwrapped phase ($\Delta\varphi_{ifg}^{x,i,j}$) of pixel x in an interferogram with master acquisition t_i and slave acquisition t_j ($t_j > t_i$) can be written as (Hanssen, 2001; Guarneri and Tebaldini, 2007)

$$\Delta\varphi_{ifg}^{x,i,j} = \Delta\varphi_{defo}^{x,i,j} + \Delta\varphi_{topo}^{x,i,j} + \Delta\varphi_{orbit}^{x,i,j} + \Delta\varphi_{atm}^{x,i,j} + e^{x,i,j} \quad (1)$$

where x represents x th pixel in interferogram, i and j denotes the i th and j th time epoch of SAR image, respectively. $\Delta\varphi_{defo}^{x,i,j}$ represents the cumulative surface deformation between two SAR acquisitions, $\Delta\varphi_{topo}^{x,i,j}$ is the phase of land topography, $\Delta\varphi_{orbit}^{x,i,j}$ represents the phase caused by inaccurate satellite orbits, $e^{x,i,j}$ denotes the noise components including the system thermal noise, decorrelation noise, co-registration noise and processing noise, $\Delta\varphi_{atm}^{x,i,j}$ is the phase of the atmospheric delay difference. The atmospheric delay includes the hydrostatic part and the non-hydrostatic part. The hydrostatic delay varies smoothly both in space and time domain and can be estimated with ground atmospheric

pressure and local temperature at a high accuracy. Therefore, it is not considered in this paper, and the atmospheric delay only refers to the non-hydrostatic component hereafter. The residual orbital errors can be removed by a surface trend model. The long wavelength atmosphere, a part of the non-hydrostatic component, with a characteristic similar to that of the orbit error, may also be removed. Therefore, the atmospheric delay used for water vapor mapping in this study mainly consists of the short-scale component (i.e., the turbulence atmosphere) and the topography-correlated component (i.e., the vertical stratification atmosphere). In addition, the deformation term, $\Delta\varphi_{defo}^{x,i,j}$, can be removed if no ground deformation occurs. The topography contribution, $\Delta\varphi_{topo}^{x,i,j}$, can be compensated by a global DEM (e.g., SRTM DEM). However, it should be noted that some of these individual removal processes may be contaminated because of each contribution from the long wavelength hardly be separated completely.

Then, after removing the deformation phase, topographic phase, orbital error, and the hydrostatic phase of atmosphere, we can construct a linear model for each pixel as

$$\Delta\varphi^{x,i,j} = \phi_{atm}^x(t_j) - \phi_{atm}^x(t_i) + e^x \quad (2)$$

which can be written in the matrix form:

$$Y = AX + e \quad (3)$$

where Y is the $M \times 1$ observation vector containing unwrapped interferometric phases, X is the $N \times 1$ unknown parameter vector, which contains the unknown water vapor at the epoch of each SAR acquisition. A is a design matrix with dimensions $M \times N$. If we adopt the older SAR image as the master, matrix A fills each row with -1 for the master epoch (t_i) and 1 for the slave epoch (t_j), and zeros for the rest epochs, resulting in

$$A = \begin{bmatrix} -1 & 1 & 0 & 0 & \cdots & 0 \\ 0 & -1 & 0 & 1 & \cdots & 0 \\ \vdots & \vdots & \vdots & \vdots & \ddots & \vdots \\ 0 & 0 & 0 & -1 & \cdots & 1 \end{bmatrix}$$

whereas the functional model relates observations with unknown parameters, the stochastic model characterizes the priori precision of the observations by its variance-covariance matrix. This characterization directly affects the estimation precision of unknown parameters. The stochastic model can be defined as (Hanssen, 2001)

$$D_{YY} = \sigma_0^2 Q_{YY} \quad (4)$$

where D_{YY} is the covariance matrix of the time-series observations, σ_0^2 is the a priori variance factor, and Q_{YY} is the relative cofactor matrix, which can be determined from the observation noise.

Assuming the N SAR acquisitions constitute only one small baseline subset, there are only $N - 1$ independent interferograms, since the M interferograms are formed from the N acquisitions. So the rest $M - (N - 1)$ interferograms can be obtained via the linear combination of the $N - 1$ independent interferograms. Therefore, the rank of the design matrix A in Eq. (3) is

$$\text{rank}(A) = N - 1 \quad (5)$$

Since the number of unknown parameters is N , greater than the number of independent equations, the linear system in Eq. (3) is rank-deficient. In other words, it will have infinite solutions.

3. Non-differential water vapor estimation under traditional constraints

In order to get a mathematically unique solution with clear physical significance, one or more constraints should be adopted in estimating the non-differential water vapor using the Gauss-Markov model.

3.1. General constraint

Assume the general constraint is

$$\mathbf{G}^T \mathbf{X} - \mathbf{W}_g = 0 \quad (6)$$

where \mathbf{G}^T is the coefficient of \mathbf{X} and \mathbf{W}_g is the constant term. Meanwhile, dimensions of \mathbf{G}^T and \mathbf{W}_g is $M_0 \times N$ and $M_0 \times 1$ (M_0 is the number of constraint equation), respectively. Combined with the general constraint (i.e., Eq. (6)), Eq. (3) can be written as

$$\begin{cases} \mathbf{Y} = \mathbf{AX} + \mathbf{e} \\ \mathbf{G}^T \mathbf{X} - \mathbf{W}_g = 0 \end{cases} \quad (7)$$

Simplified as

$$\mathbf{Y}_{total} = \mathbf{A}_{total} \mathbf{X} + \mathbf{e}_{total} \quad (8)$$

where $\mathbf{Y}_{total} = \begin{bmatrix} \mathbf{Y} \\ \mathbf{W}_g \end{bmatrix}$, $\mathbf{A}_{total} = \begin{bmatrix} \mathbf{A} \\ \mathbf{G}^T \end{bmatrix}$ and $\mathbf{e}_{total} = \begin{bmatrix} \mathbf{e} \\ \mathbf{0} \end{bmatrix}$. Meanwhile, the dimensions of \mathbf{Y}_{total} , \mathbf{A}_{total} and \mathbf{e}_{total} is $(M + M_0) \times 1$, $(M + M_0) \times N$ and $(M + M_0) \times 1$, respectively. Besides that, the number of equations (i.e., $M + M_0$) is larger than the number of unknown parameters (i.e., N) in Eq. (8) by using SBAS-InSAR algorithm and the coefficient matrix (i.e., \mathbf{A}_{total}) is full rank. This means Eq. (8) is referred to as an overdetermined system and widely be solved by the weighted least-squares (WLS) method (Teunissen et al., 2008). However, the principle of the WLS algorithm is searching $\hat{\mathbf{X}}$ to make the squared norm of the least-squares residual vector being minimum, namely $\mathbf{V}_{total}^T \mathbf{P}_{total} \mathbf{V}_{total}$ is minimum. The matrix \mathbf{P}_{total} represents the weight of matrix \mathbf{Y}_{total} and \mathbf{V}_{total} denotes the least-squares residual vector which be defined as the difference between $\mathbf{A}_{total} \mathbf{X}$ and $\mathbf{A}_{total} \hat{\mathbf{X}}$:

$$\mathbf{V}_{total} = \mathbf{A}_{total} \mathbf{X} - \mathbf{A}_{total} \hat{\mathbf{X}} \quad (9)$$

where $\hat{\mathbf{X}}$ is the estimator of \mathbf{X} . Then, under this condition, the WLS solution of \mathbf{X} can be computed from \mathbf{Y}_{total} , \mathbf{A}_{total} and \mathbf{Q}_{total} as

$$\begin{aligned} \hat{\mathbf{X}} &= (\mathbf{A}_{total}^T \mathbf{Q}_{total}^{-1} \mathbf{A}_{total})^{-1} \mathbf{A}_{total}^T \mathbf{Q}_{total}^{-1} \mathbf{Y}_{total} \\ &= \left(\begin{bmatrix} \mathbf{A} \\ \mathbf{G}^T \end{bmatrix}^T \begin{bmatrix} \mathbf{Q}_{11} & \mathbf{Q}_{12} \\ \mathbf{Q}_{21} & \mathbf{Q}_{22} \end{bmatrix}^{-1} \begin{bmatrix} \mathbf{A} \\ \mathbf{G}^T \end{bmatrix} \right)^{-1} \begin{bmatrix} \mathbf{A} \\ \mathbf{G}^T \end{bmatrix}^T \begin{bmatrix} \mathbf{Q}_{11} & \mathbf{Q}_{12} \\ \mathbf{Q}_{21} & \mathbf{Q}_{22} \end{bmatrix}^{-1} \begin{bmatrix} \mathbf{Y} \\ \mathbf{W}_g \end{bmatrix} \end{aligned} \quad (10)$$

where \mathbf{Q}_{total} is the total variance and covariance matrix for Eq. (8) and $\mathbf{Q}_{total} = \begin{bmatrix} \mathbf{Q}_{11} & \mathbf{Q}_{12} \\ \mathbf{Q}_{21} & \mathbf{Q}_{22} \end{bmatrix}$, \mathbf{Q}_{11} and \mathbf{Q}_{22} is the variance and covariance matrix for Eq. (3) and Eq. (6), respectively. \mathbf{Q}_{12} equals to \mathbf{Q}_{21} and represents the covariance matrix between Eq. (3) and Eq. (6).

The matrix \mathbf{Q}_{total} not only depends on the noises in interferograms, such as decorrelation noise, co-registration noise and data processing noise, but also depends on the measurement accuracy of the added constraint. However, these are hard to estimate by using a deterministic model as present. Therefore, \mathbf{Q}_{total} is simply taken as the identity matrix in this research. Then, the WLS solution of \mathbf{X} can be simplified as

$$\hat{\mathbf{X}} = (\mathbf{A}^T \mathbf{A} + \mathbf{G} \mathbf{G}^T)^{-1} (\mathbf{A}^T \mathbf{Y} + \mathbf{G} \mathbf{W}_g) \quad (11)$$

3.2. One or more epoch's water vapor being known

Using one or more external water vapor measurements (e.g. from MERIS) acquired during the same period with the SAR acquisitions is the easiest constraint method for estimating non-differential water vapor (Pichelli et al., 2015; Duan, 2016; Mateus et al., 2017). We refer it as 'One-epoch Known Constraint' hereinafter. In this case, $\mathbf{G}^T = (0, \dots, 1, \dots, 1, 0)$, and 1 represents the position of external water vapor measurements in SAR image time series. The number of "1" represents the number of known water vapor images.

However, each interferogram participating in non-differential water

vapor mapping certainly contains various noises (e.g., data processing noise, thermal noise, spatial-temporal decoherence noise). Therefore, based on the theory of error diffusion, the smaller the time interval between the known water vapor image and the unknown epoch image, the higher the estimation accuracy. Generally, the number of known water vapor images and their corresponding positions in the SAR image time series are the main factors influencing water vapor estimation. Large number of water vapor images with discrete distributions in time series will increase the estimation precision. In addition, redundant observations also can improve the accuracy.

3.3. The temporal mean of water vapor being zero

As the *One-epoch Known Constraint* is a local constraint, Alshawaf et al. (2015) adopted the temporal mean of water vapor being zero as the global constraint to estimate the non-differential water vapor. We refer it as 'Zero-Mean Constraint' hereafter.

According to this constraint, Eq. (3) can be modified to:

$$\begin{cases} \mathbf{Y} = \mathbf{AX} + \mathbf{e} \\ \mathbf{G}^T \mathbf{X} = 0 \end{cases} \quad (12)$$

where the dimension of \mathbf{G}^T is $1 \times M$ and $\mathbf{G}^T = (1/N, 1/N, \dots, 1/N)$ and $\mathbf{W}_g = 0$. The least squares solution of \mathbf{X} in Eq. (12) is

$$\hat{\mathbf{X}} = (\mathbf{A}^T \mathbf{A} + \mathbf{G} \mathbf{G}^T)^{-1} \mathbf{A}^T \mathbf{Y} \quad (13)$$

Since seasonal variations have great effects on the statistics of the turbulence atmospheric signals, we should ensure that the starting and the ending SAR images of our dataset were obtained in similar seasons. Meanwhile, the vertical atmosphere, a function of the surface height, may have an effect on the statistics of the turbulence atmosphere. Therefore, this constraint does not work well in regions where the topography is highly or even modestly uneven.

More importantly, this method requires a sufficient number of SAR images to ensure the whole estimation precision. In summary, the difference between the actual value of temporal mean of water vapor and zero is the key factor that affects the precision of water vapor estimation. Hence, the larger the number of SAR images, the closer the actual value of temporal mean of water vapor to zero, the more interferograms, and the higher the water vapor estimation precision.

4. Non-differential water vapor estimation under new constraint

4.1. The temporal mean of water vapor being invariant

As stated in Section 3.3, the *Zero-Mean Constraint* isn't suitable for the area with strong topographic reliefs, because of the dominant stratified atmosphere. Even for flat areas, the number of SAR images and extreme weather may lead to a bias in the estimated result. To avoid these, we propose a new constraint, the temporal mean of water vapor being invariant

$$\mathbf{G}^T \mathbf{X} = \mathbf{K} \quad (14)$$

where \mathbf{K} is the temporal mean of water vapor in time series. This constraint is referred as '*Invariant-Mean Constraint*' hereinafter. We will develop the method to estimate water vapor under this constraint in the following section, and discuss how to evaluate the temporal mean of water vapor in Section 6.3.

4.2. Non-differential water vapor estimation under the new constraint

Based on the *Invariant-Mean Constraint*, Eq. (3) can be rewritten as

$$\begin{cases} \mathbf{Y} = \mathbf{AX} + \mathbf{e} \\ \mathbf{G}^T \mathbf{X} = \mathbf{K} \end{cases} \quad (15)$$

where, the dimension of G^T is $1 \times M$ and $G^T = (1/N, 1/N, \dots, 1/N)$ and $W_g = K$. K is the temporal mean of water vapor in time series at each pixel.

Then, the least squares solution of X in Eq. (15) is given as

$$\hat{X} = (A^T A + G G^T)^{-1} (A^T Y + G K) \quad (16)$$

with the new constraint (i.e., the *Invariant-Mean Constraint*), the unknown water vapor at the epoch of each SAR acquisition can be obtained by Eq. (16). Meanwhile, it can ensure the whole estimation precision of water vapor from TS-InSAR. Furthermore, if there is no error in the temporal mean of water vapor in time series, the only factor influencing the accuracy is the number of interferogram.

5. Experiments and analysis

5.1. Synthetic test

5.1.1. Simulation

Five independent SAR images are simulated with a spatial dimension of 256 pixel \times 256 pixel. As the *Zero-Mean Constraint* method is based on the stochastic characteristic of the turbulent atmosphere, we assume the research area has no surface height change, and simulate the turbulent tropospheric signal for each SAR acquisition by the Kolmogorov turbulence theory (Hanssen, 2001; González and Fernandez, 2011; Cao et al., 2017). As stated in Section 2.1, the deformation phase can be removed from the unwrapped interferograms completely, so we neglect the ground deformation in the experiment. In addition, we simulate the decorrelation noise based on four factors: coregistration induced decorrelation, geometric decorrelation, thermal decorrelation and temporal decorrelation (Rocca, 2007; Samiei, 2017). Subsequently, seven interferograms are generated by differentiating the simulated image at master and slave epochs and the corresponding

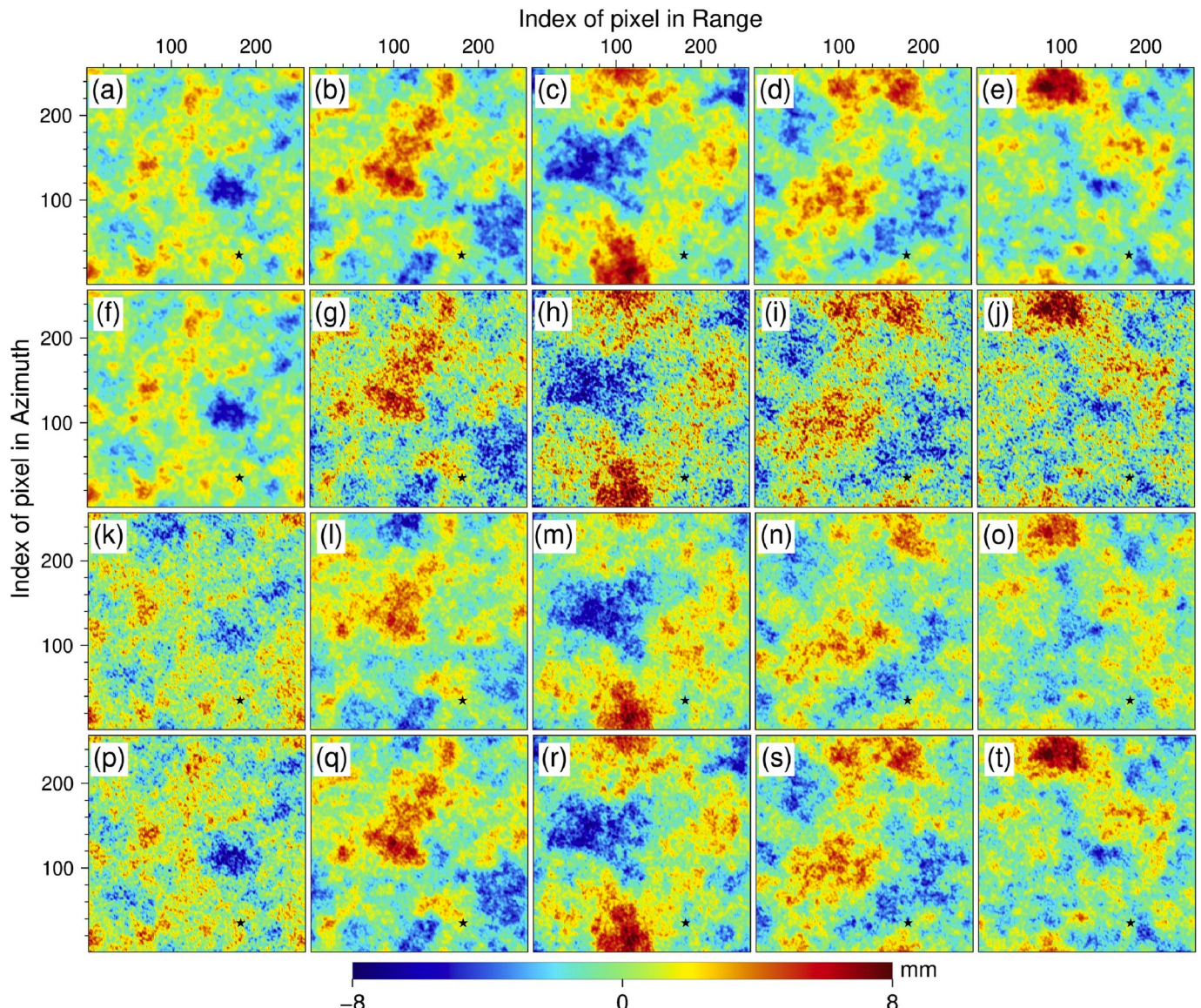


Fig. 1. The simulated and estimated PWVs corresponding to the five simulated SAR acquisitions. The black star denotes the reference point. (a)–(e) Simulated PWVs. (f)–(j) PWVs estimated under the *One-epoch Known Constraint*. (k)–(o) PWVs estimated under the *Zero-Mean Constraint*. (p)–(t) PWVs estimated under the *Invariant-Mean Constraint*.

temporal-spatial baseline distribution is the same as the real experiment in Section 5.2. Finally, we take the time series of unwrapped phases as the input data for the constraint method. Therefore, the phase unwrapping error is not considered.

5.1.2. Non-differential water vapor estimation results

In view of the *One-epoch Known Constraint*, without loss of generality, we assume the water vapor of the first image is known and the rest are unknown. Estimated results based on the three constraints are shown in Fig. 1.

As Fig. 1 shows, all the three constraints retrieve PWVs in time series, but the *One-epoch Known Constraint* generates results (i.e., Fig. 1(f)–(j)) with much more noises than the other two constraints (i.e., Fig. 1(k)–(o) and Fig. 1(p)–(t), respectively). Meanwhile, the first epochs of the results of *Zero-Mean Constraint* and the *Invariant-Mean Constraint* (i.e., Fig. 1(k) and (p)) contain more noise than the other four epochs. To further demonstrate the performances of these three constraints in water vapor mapping, we calculate the differences between the simulated PWVs and the estimated PWVs based on the three constraints (Fig. 2).

As presented in Fig. 2, the differences in the third row (i.e., the differences between the simulated and the estimated PWVs under the *Invariant-Mean Constraint*) are the minimum. Among them, Fig. 2(k) contains more noise than the other four epochs (i.e., Fig. 2(l)–(o)), which may be due to the first simulated image participated in the least number of interferograms, leading to minimum redundant observations. The results in the first row (i.e., Fig. 2(a)–(e)) contain relatively complex noises. And there are obvious deviations in the second row (i.e., Fig. 2(f)–(j)). Therefore, the *One-epoch Known Constraint* and the *Zero-Mean Constraint* have relatively poorer performance than the *Invariant-Mean Constraint*.

Constraint.

5.2. Real data test

5.2.1. SAR data and processing

We select Jeddah, Saudi Arabia, as the experimental area. Most of months in this area are very dry except from November to January. This is helpful to obtain high-quality MERIS image which is particularly vulnerable to be contaminated by cloud and be used for verifying the estimations, simultaneously. And five descending Envisat/Advanced SAR (ASAR) images were acquired over this region from 27 November 2007 to 29 July 2008. Seven interferograms with average temporal baseline of 70 days and perpendicular baseline of 205 m are generated from the five ASAR images (see Fig. 3). Multi-look processing with four pixels in range and twenty pixels in azimuth is used to produce interferograms with a pixel size of approximately 80 m × 80 m. Subsequently, the topography phase is removed through the two-pass D-InSAR procedure (Massonnet et al., 1993) using an external DEM (30 m) from the Shuttle Radar Topography Mission (SRTM). The precise orbit information from Delft Institute for Earth-Oriented Space Research is utilized to minimize orbital errors. Residual orbit errors are modeled as a surface trend and are mitigated from the unwrapped phase. To reduce the influence of noise, each interferogram is filtered by the improved Goldstein filter (Li et al., 2008). In addition, since the study area is stable (Smith, 2012) and the spatial-temporal baseline is small, the deformation phase in this area can be neglected. Furthermore, pixels with coherence less than 0.6 are masked out in the time-series analysis to ensure a high quality solution. In the end, the residual differential phase (i.e., $\Delta\phi$ in Eq. (17)) in LOS is converted to the differential PWV (i.e.,

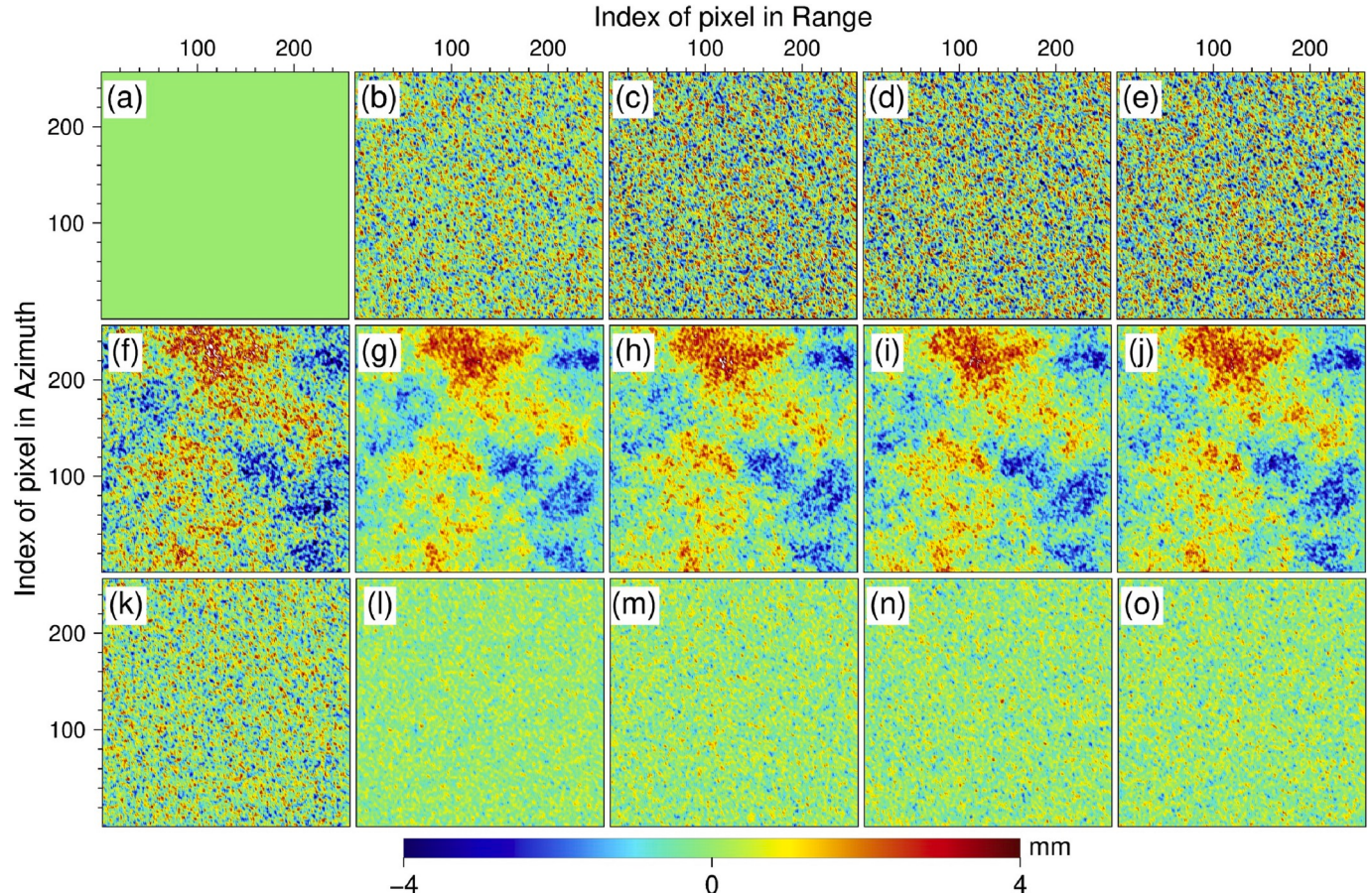


Fig. 2. Differences between the simulated and the estimated PWVs (corresponding to the five simulated SAR acquisitions) under (a)–(e) the *One-epoch Known Constraint*, (f)–(j) the *Zero-Mean Constraint* and (k)–(o) the *Invariant-Mean Constraint*.

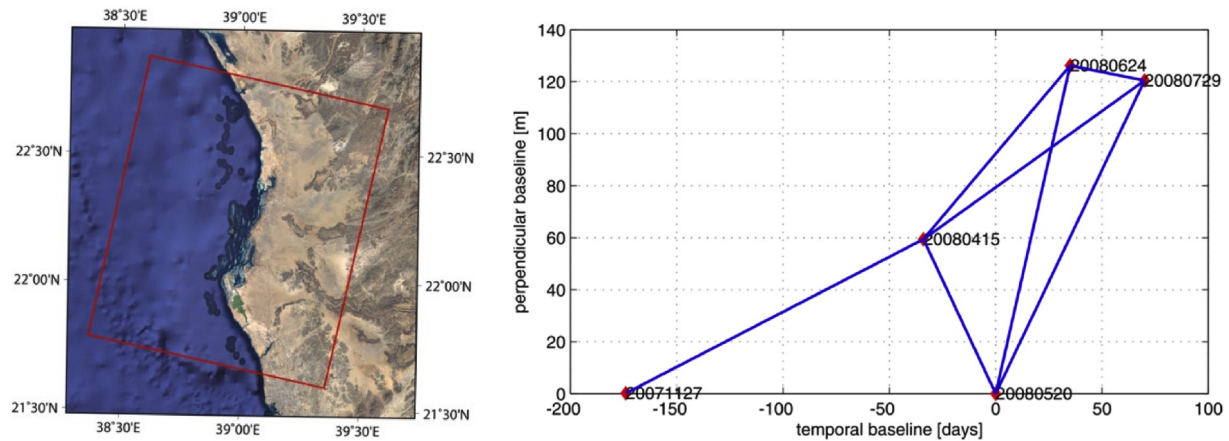


Fig. 3. The red rectangle represents the coverage of the ASAR frame (left). Baseline plot of the ASAR acquisitions used in the case study (right). Each node represents an ASAR acquisition and each edge connecting two nodes represents the interferogram formed by the two acquisitions. (For interpretation of the references to colour in this figure legend, the reader is referred to the Web version of this article.)

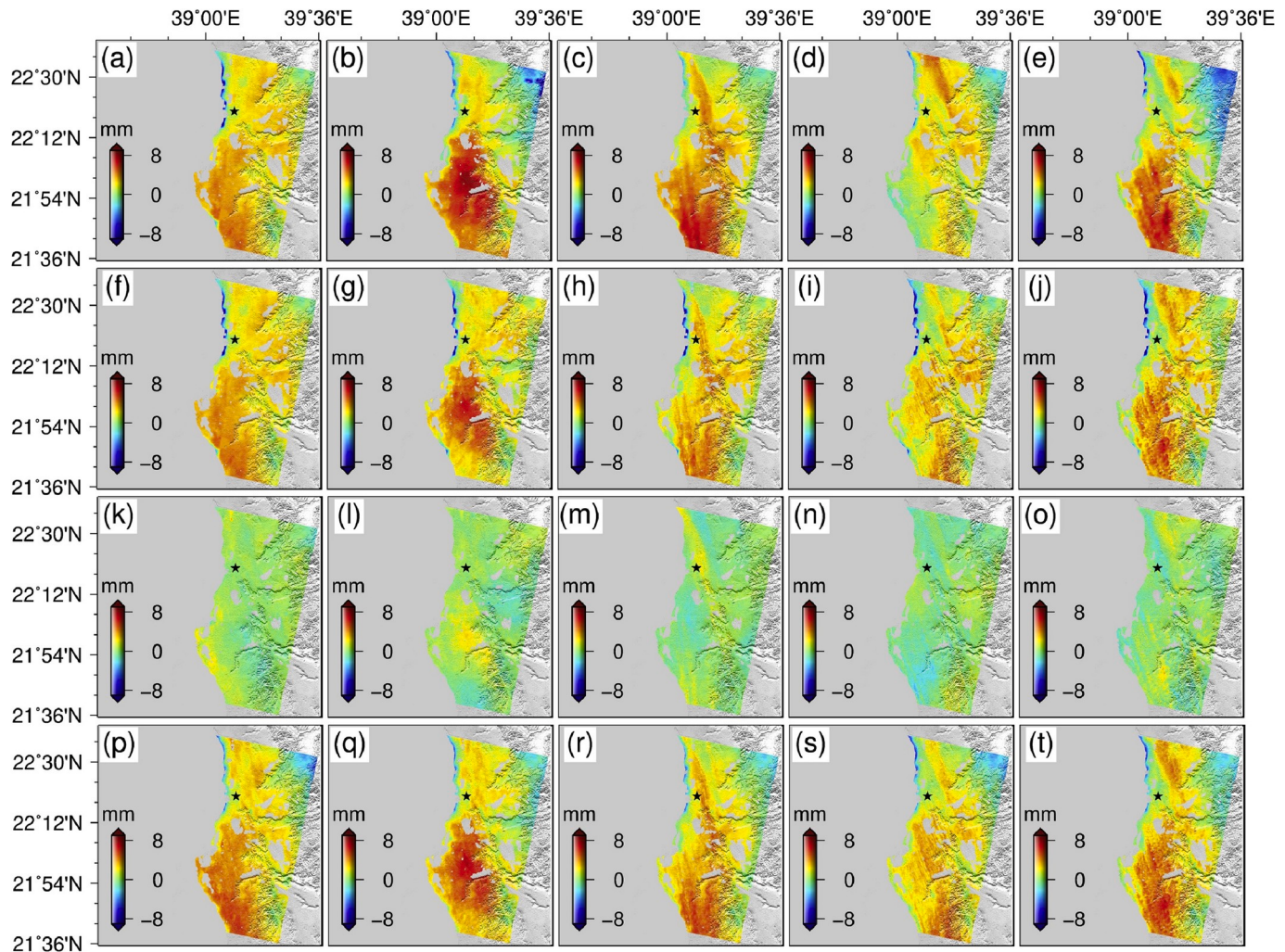


Fig. 4. The MERIS and the estimated PWVs of the five SAR acquisitions. (a)–(e) MERIS PWVs. The black star denotes reference point in the unwrapped interferograms. (f)–(j) PWVs estimated under the *One-epoch Known Constraint*. (k)–(o) PWVs estimated under the *Zero-Mean Constraint*. (p)–(t) PWVs estimated under the *Invariant-Mean Constraint*.

ΔPWV in Eq. (17)) by (Mateus et al., 2011):

$$\Delta\text{PWV} = \Pi \frac{-\lambda}{4\pi} \Delta\phi \cos\theta \quad (17)$$

where Π is the water vapor conversion factor, λ is the radar wave length, $\Delta\phi$ is the differential phase, and θ is the incidence angle.

5.2.2. MERIS data and processing

The Envisat satellite is equipped with a Medium Resolution Imaging Spectrometer (MERIS), which enables the simultaneous collection of PWV and SAR data. MERIS final near-infrared water vapor products are provided at two nominal spatial resolutions, i.e., 0.3 km for the full resolution model and 1.2 km for the reduced resolution mode. Bennartz and Fischer (2001) reported that the theoretical accuracy of the water vapor retrieval from MERIS could be as high as 1.7 mm under cloud-free conditions. However, the MERIS derived PWV is prone to clouds. Although the cloud cover is rare in this study area, we can only collect five cloudless synchronized MERIS images for this study. We use them as the reference in the following analysis and take their average as the temporal mean.

5.2.3. Non-differential water vapor estimation results

Similar to the synthetic test, we assume the PWV of the first image being known and the rest unknown. Then, we use the above generated interferograms to build maps of PWV in time series. The PWVs derived from MERIS are shown in Fig. 4(a)-(e). The second, third and fourth rows of Fig. 4 are the PWVs estimated under the *One-epoch Known Constraint*, the *Zero-Mean Constraint*, and the *Invariant-Mean Constraint*, respectively.

As shown in Fig. 4, the estimated PWVs in the second and fourth rows are similar to the first row. The PWVs in the third row are relatively poor and can hardly reconstruct the true PWVs, indicating that the *Zero-Mean Constraint* does not work well in estimating PWV. The results of the fourth row have higher consistency with the first row than the second

row does on the whole. Therefore, the *Invariant-Mean Constraint* retrieves the PWV with the highest accuracy, followed by the *One-epoch Known Constraint*, then the *Zero-Mean Constraint* results. There are some discrepancies between the PWVs estimated under the *One-epoch Known Constraint*, the *Invariant-Mean Constraint* and by MERIS, especially of the fourth image (i.e., Fig. 4(d), (i), (s)). These discrepancies might be caused by the cloud masking errors of MERIS. Note that, using a surface trend can remove the residual orbital errors, and even some atmospheric signals, especially the long wavelength atmosphere. How to completely remove the orbit errors from interferograms and has no influence on the atmospheric signals needs further research.

We calculate the differences between the PWV from MERIS and that from the three constraints (Fig. 5). As the figure shows, the third row has the minimum differences on the whole, followed by the first row. This means the result with the *Invariant-Mean Constraint* are in good agreement with MERIS. However, there are obvious deviations in the second row, which indicates the bad performance of the *Zero-Mean Constraint*. Furthermore, we find that there is a weak similarity between the PWVs derived from MERIS (i.e., Fig. 4(a)-(e)) and the residuals from the *Invariant-Mean Constraint* (i.e., Fig. 5(k)-(o)). It indicates different degrees of PWV deficit in the estimation by using the *Invariant-Mean Constraint* at each SAR imaging epoch. It might be caused by the identity weighting assumed in this research for simplification.

Fig. 6 shows the histogram of the frequency distributions of the differences between the PWVs derived from MERIS and that with the three constraints. In the first and third rows, 6(a)-(e) and Fig. 6(k)-(o), the differences follow a Gaussian distribution with mean values close to zero and standard deviations less than 2 mm. While in the second row, i.e., Fig. 6(f)-(j), the differences are larger. In addition, the PWVs under the *Invariant-Mean Constraint* have an average improvement of 42.0% and 81.8% over that estimated under the *One-epoch Known Constraint* and the *Zero-Mean Constraint*, respectively.

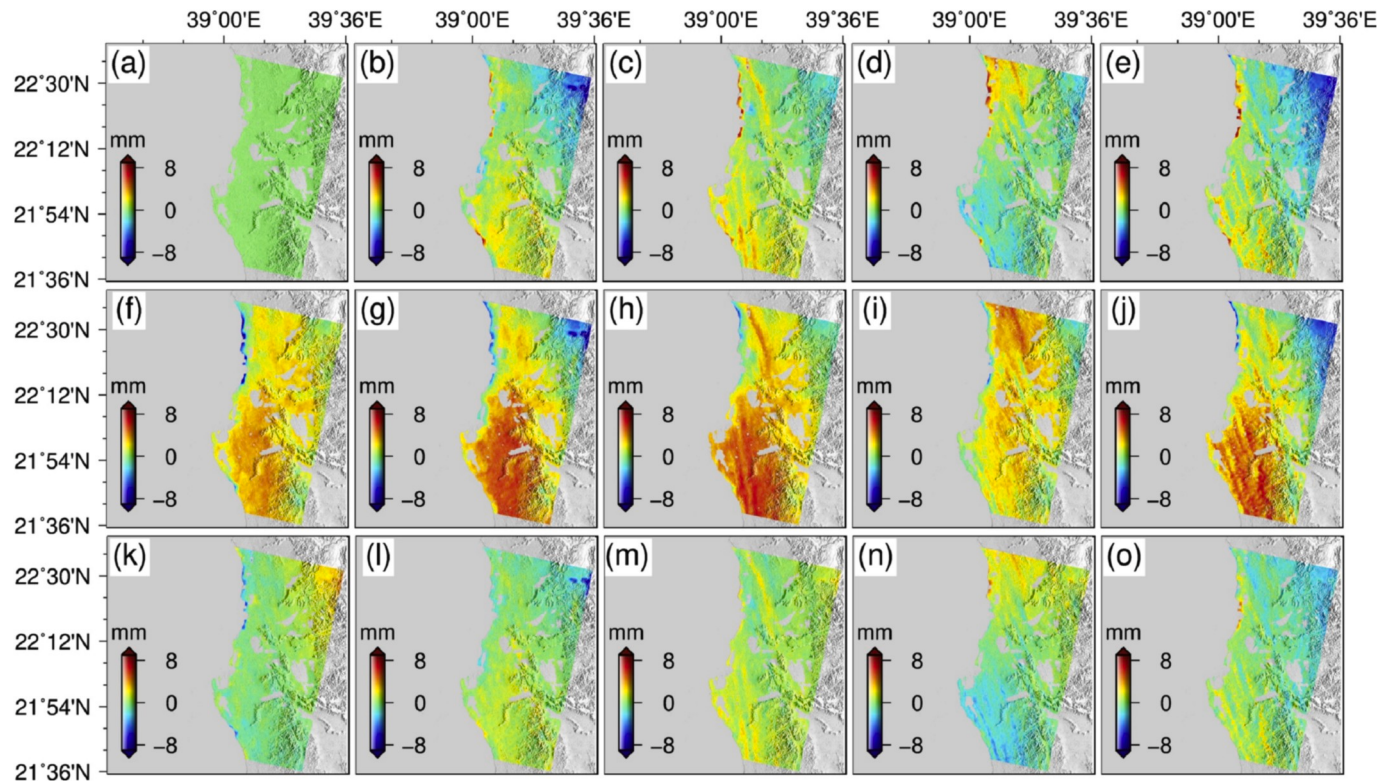


Fig. 5. Differences between the MERIS and the estimated PWVs under (a)–(e) the *One-epoch Known Constraint*, (f)–(j) the *Zero-Mean Constraint* and (k)–(o) the *Invariant-Mean Constraint*.

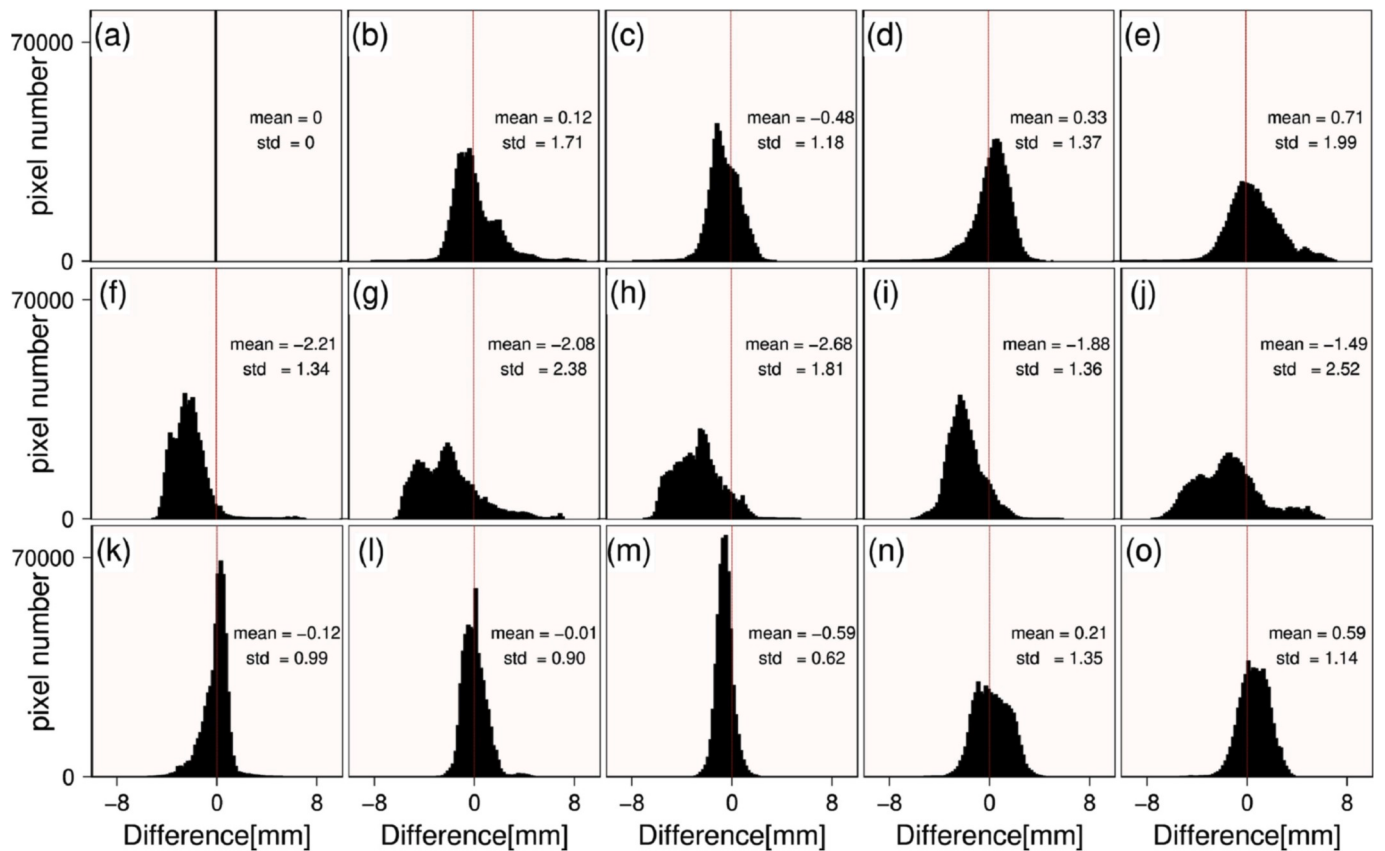


Fig. 6. Histogram of the differences between the PWVs derived from MERIS and estimated under (a)–(e) the *One-epoch Known Constraint*, (f)–(j) the *Zero-Mean Constraint*, and (k)–(o) the *Invariant-Mean Constraint*, respectively.

6. Discussion

6.1. Constant bias between the solutions under the Invariant-Mean Constraint and the Zero-Mean Constraint

It is expected that biases would increase between the PWVs estimated from TS-InSAR under the *Zero-Mean Constraint* and *Invariant-Mean Constraint*. However, how large the biases and in what way they propagate remain unknown. Hence, we investigate the differences between the results.

Firstly, according to the least squares solutions under these two constraints (i.e., Eq. (13) and Eq. (16)), the difference of the estimated PWVs (i.e., $\Delta\hat{X}$) can be written as:

$$\Delta\hat{X} = (A^T A + GG^T)^{-1} G K \quad (18)$$

The sum of each row of the real symmetric matrix $(A^T A + GG^T)$ is $1/N$, so $1/N$ is an eigenvalue of $(A^T A + GG^T)$ and the corresponding eigenvector is $[1, 1, \dots, 1]$. Therefore, N is an eigenvalue of the real symmetric matrix $(A^T A + GG^T)^{-1}$ and the corresponding eigenvector is $[1, 1, \dots, 1]$. That means the sum of all the elements in each row of $(A^T A + GG^T)^{-1}$ is N . In such a case, Eq. (18) can be simplified to:

$$\Delta\hat{X} = K \quad (19)$$

From Eq. (19), we can see that the bias is a constant and equals to the temporal mean. It demonstrates that the *Zero-Mean Constraint* may lead to a constant bias in the estimated water vapor compared with the new constraint. Meanwhile, this conclusion can be used to illustrate the almost same residuals from the *Zero-Mean Constraint* method both in simulation (i.e., Fig. 2(f)–(j)) and real data experiments (i.e., Fig. 5(f)–(j)). Besides, unlike the *Zero-Mean Constraint*, the performance of

Invariant-Mean Constraint isn't affected by the number of SAR images, terrain and extreme weathers.

6.2. Equivalency between the solutions under the Invariant-Mean Constraint and the rule of minimum-norm least-squares

Results of the simulated and real experiments show that the solution under the new constraint has a higher accuracy than that under the other two constraints. We also calculate the correlations between the PWVs estimated under the three constraints and that derived by MERIS (Table 1). The correlation value is as high as 0.95 and with an average of 0.86 between the results under *Invariant-Mean Constraint* and of MERIS, indicating that the PWV spatial distribution estimated under this constraint is almost consistent with the MERIS PWV. The equivalent values for the *One-epoch Known Constraint* is lower. Meanwhile, it should be noted that the PWV of the first image has been assumed known for the *One-epoch Known Constraint* as stated in Section 5.2.3. Therefore, the correlation is as high as 1.00 for the *One-epoch Known Constraint* case 1, as shown in Table 1. The results under the *Zero-Mean Constraint* has the correlation as low as 0.21 and with an average of 0.27, suggesting that the results are seriously biased.

As mentioned in Section 3.1, the constraint should be independent to the observation equation (i.e., Eq. (3)). Therefore

Table 1

Correlation between the PWVs estimated under the three constraints and that derived by MERIS (corresponding to the five SAR acquisitions).

Constraint Applied	1	2	3	4	5
<i>One-epoch Known Constraint</i>	1.00	0.73	0.76	0.53	0.65
<i>Zero-Mean Constraint</i>	0.26	0.32	0.21	0.27	0.28
<i>Invariant-Mean Constraint</i>	0.84	0.95	0.94	0.63	0.92

$$\mathbf{A} \cdot \mathbf{G} = 0 \quad (20)$$

The real-symmetric matrix $\mathbf{A}^T \mathbf{A}$ is not full rank, thus at least one eigenvalue of $\mathbf{A}^T \mathbf{A}$ is equal to zero and the corresponding eigenvector is \mathbf{R}^T . So we have

$$\mathbf{A}^T \mathbf{H} = h \mathbf{A}^T \mathbf{A} = 0 \quad (21)$$

where h equals to zero and is the eigenvalues of the real-symmetric matrix. The matrix \mathbf{H} is the corresponding eigenvector. Meanwhile, according to Eq. (10), $\hat{\mathbf{X}}$ is WLS solution of \mathbf{X} . Therefore, the estimation error of parameter \mathbf{X} is:

$$\hat{\mathbf{x}} = \hat{\mathbf{X}} - \mathbf{X} \quad (22)$$

where $\hat{\mathbf{x}}$ is the estimation error of parameter \mathbf{X} . Then, let $\mathbf{Z} = (\mathbf{A}^T \mathbf{A} + \mathbf{G} \mathbf{G}^T)^{-1}$, and combine Eqs. (7)–(9), we can get:

$$\hat{\mathbf{x}}^T \hat{\mathbf{x}} = \mathbf{y}^T \mathbf{A} \mathbf{Z} \mathbf{Z}^T \mathbf{A}^T \mathbf{y} + \mathbf{w}^T (\mathbf{G}^T \mathbf{G})^{-1} \mathbf{w} \quad (23)$$

where \mathbf{y} and \mathbf{w} is the observation error of \mathbf{Y} and \mathbf{W}_g , respectively.

Under the *Invariant-Mean Constraint*, one gets

$$\frac{1}{N} \sum_{k=1}^N (X_k + \hat{X}_k) = \frac{1}{N} \sum_{k=1}^N X_k \quad (24)$$

It can be simplified to

$$\frac{1}{N} \sum_{k=1}^N \hat{X}_k = 0 \quad (25)$$

which is equivalent to:

$$\left\{ \begin{array}{l} \mathbf{G}^T = \left(\frac{1}{N}, \frac{1}{N}, \dots, \frac{1}{N} \right) \\ w = 0 \end{array} \right. \quad (26)$$

Under this constraint, $\hat{\mathbf{x}}^T \hat{\mathbf{x}}$ in Eq. (23) would be the minimum. This demonstrates the equivalency between the solutions under the *Invariant-Mean Constraint* and that obtained by the minimum-norm least-square. As the other two constraints cannot meet the $\hat{\mathbf{x}}^T \hat{\mathbf{x}}$ minimum, their results are not optimal. This also proves that the water vapor estimated under the proposed constraint has the highest precision.

6.3. General comparison, model selection and consideration for application

The *One-epoch Known Constraint* method has great advantages of small calculation load and easy programming. But knowing one or more epoch's water vapor is the premise of this method. Furthermore, it cannot ensure the global accuracy in time series. Thus, when the number of SAR image is limited and the amount of external water vapor is large, this method can be used to estimate non-differential water vapor from SBAS-InSAR.

The *Zero-Mean Constraint* can be used to map the non-differential water vapor, if there are a sufficient number of SAR images for a given region without any surface deformation. This method also has low calculation cost and easy computer programming. But it is easily affected by weathers, especially extreme weathers. Besides, as stated in Section 6.1, its results have a constant bias.

As proved in Section 6.2, the *Invariant-Mean Constraint* provides the highest estimation accuracy among these three constraints. In addition, it is not influenced by the number of SAR image and the terrain of study area. Meanwhile, the calculation of this constraint is also simple. However, this constraint also has its drawback, which is the prior determination of the temporal mean of the study area. With relatively higher spatial resolution and accuracy, spectrometer observations (e.g., MODIS and MERIS), especially MERIS, maybe the preferred method to

obtain the temporal mean of water vapor. However, both MODIS and MERIS images are prone to clouds and are only available during the daytime. Fortunately, previous studies have shown that numerical weather models can be a promising tool for computing the temporal mean of water vapor under any weather condition (Wadge et al., 2002; Foster et al., 2006; Puysségur et al., 2007; Gong et al., 2010; Wang et al., 2017). Whereas, the initial and boundary parameters for numerical weather models need further research to ensure its reliability at all times and locations. The free access, daily availability and global coverage make the atmospheric reanalysis products be widely used to obtain the temporal mean of water vapor. But their spatial resolution is low at present. Maybe, we can obtain the temporal mean of water vapor by combining atmospheric reanalysis products, GNSS, spectrometer observations and numerical weather models (Chang and He, 2011; Mengistu et al., 2015; Chen and Liu, 2016). However, the temporal mean of water vapor with high spatial resolutions cannot always be obtained by these methods. In addition, there are measurement errors in the estimated temporal mean of water vapor (i.e., K in Eq. (15)). Therefore, a comprehensive study on the influence of the measuring precision of the temporal mean on PWVs estimation is needed. In fact, the *Zero-Mean Constraint* is a special case of the *Invariant-Mean Constraint*. Under this case, the error of the temporal mean of water vapor (i.e., K in Eq. (15)) equals to the real temporal mean of water vapor in time series, and the corresponding error of the estimated non-differential water vapor is also equivalent to the real temporal mean of water vapor.

Several other factors also affect the three constraints. First, the number and distribution of interferograms, which affects the matrix \mathbf{A} in Eq. (3), determine the model and data resolution of time series water vapor mapping. Second, even we assume the ground deformation being known or can be negligible, the decorrelation noise, the thermal noise and the processing noise (e.g., co-registration and unwrapping noise) both can influence the precision of the result. At last, we assume that the orbital error can be removed by an empirical mathematical model (e.g., plane model, quadratic function), so the long-wavelength atmospheric signals with a similar trend may be removed, too. To keep the long-wavelength atmospheric signals, one option is to use SAR systems with reliable orbital parameters (e.g., TerraSAR-X, ALOS-2). The other method is to model the differences between $\Delta \text{PWV}_{\text{InSAR}}$ (i.e., ΔPWV derived from InSAR) and $\Delta \text{PWV}_{\text{external}}$ (i.e., ΔPWV derived from external source, such as GNSS, MERIS), and then to compensate the long-wavelength atmospheric signals in the unwrapped phase (Pichelli et al., 2015; Mateus et al., 2017).

7. Conclusion

High spatial resolution atmospheric PWV is important for recognizing local variations of the water vapor spatial distribution and may contribute to the atmospheric error corrections of certain remote sensing applications based on radio frequency measurements. Currently, measurements by ground-based and upper-air sounding networks furnish the PWV distribution only at a coarse scale, which cannot capture the variations of the local water vapor. InSAR technique, however, could provide the differential water vapor between two SAR images (i.e., ΔPWV) with a high spatial resolution over a wide swath. However, as we have pointed out in Section 2, there is rank deficiency when it is used in mapping the water vapor corresponding to each SAR image (i.e., the non-differential water vapor).

In this study, we formulate a general framework for non-differential water vapor estimation from SBAS-InSAR. After prove that the bias caused by the *Zero-Mean Constraint* is a constant that equals to the temporal mean, we propose the *Invariant-Mean Constraint* and develop the corresponding water vapor inversion method to compensate this bias. Furthermore, we demonstrate the equivalency between the solutions under the *Invariant-Mean Constraint* and that obtained by the minimum-norm least-squares. This indicates that the *Invariant-Mean Constraint* can provide a better estimation than the other two traditional

constraints. To make the method more practical and feasible, we discuss the possible methods to determine the temporal mean. General comparison, model selection and specific consideration for the application of the method developed are also discussed.

In summary, the developed general framework for non-differential water vapor estimation from SBAS-InSAR can be used to capture the small-scale water vapor distribution, with an unprecedented spatial resolution and accuracy. Those advantages of this source of non-differential water vapor can be applied to numerical weather forecasting models to enhance the accuracy of their assimilation systems. This, in turn, will help to correct the delay affected by non-differential water vapor in the space geodetic measurements.

Acknowledgments

This work was partly supported by the National Science Fund for Distinguished Young Scholars (No. 41925016), the National Key R&D Program of China (No. 2018YFC1503603), the National Natural Science Foundation of China (No. 41804008), the Leading Talents Plan of Central South University (grant number 506030101), the Primary Research & Development Plan of Hunan Province (No. 2016SK2002), the Major Projects of High Resolution Earth Observation System of China (Civil Part) (No. 03-Y20A11-9001-15/16), and the China Scholarship Council (No. 201506370139). We thank the ESA for the ENVISAT ASAR images and MERIS data used.

References

- Alshawaf, F., Hinz, S., Mayer, M., Meyer, F.J., 2015. Constructing accurate maps of atmospheric water vapor by combining interferometric synthetic aperture radar and GNSS observations. *J. Geophys. Res.: Atmos.* 120 (4), 1391–1403.
- Benevides, P., Nico, G., Fernandes, J.C., Miranda, P.M., 2016. Bridging InSAR and GPS tomography: a new differential geometrical constraint. *IEEE Trans. Geosci. Rem. Sens.* 54 (2), 697–702.
- Bennartz, R., Fischer, J., 2001. Retrieval of columnar water vapor over land from backscattered solar radiation using the Medium Resolution Imaging Spectrometer. *Remote Sens. Environ.* 78 (3), 274–283.
- Bevis, M., Businger, S., Herring, T.A., Rocken, C., Anthes, R.A., Ware, R.H., 1992. GPS meteorology: remote sensing of atmospheric water vapor using the global positioning system. *J. Geophys. Res.: Atmos.* 97 (D14), 15787–15801.
- Cao, Y.M., Li, Z.W., Wei, J.C., Hu, J., Duan, M., Feng, G.C., 2017. Stochastic modeling for time series InSAR: with emphasis on atmospheric effects. *J. Geodes.* 92 (2), 185–204.
- Chang, L., He, X.F., 2011. InSAR atmospheric distortions mitigation: GPS observations and NCEP FNL data. *J. Atmos. Sol. Terr. Phys.* 73 (4), 464–471.
- Chang, L., Liu, M., Guo, L., He, X., Gao, G., 2016. Remote sensing of atmospheric water vapor from synthetic aperture radar interferometry: case studies in Shanghai, China. *J. Appl. Remote Sens.* 10 (4), 046032.
- Chen, B.Y., Liu, Z.Z., 2016. Global water vapor variability and trend from the latest 36 year (1979 to 2014) data of ECMWF and NCEP reanalysis, radiosonde, GPS, and microwave satellite. *J. Geophys. Res.: Atmos.* 121 (19).
- Duan, M., 2016. Analysis of the constraint conditions on Non-differential water vapor inversion from InSAR Time Series. Central South University, Hunan, China.
- Duan, J.M., Bevis, M., Fang, P., Bock, Y., Chiswell, S.R., Businger, S., King, R.W., 1996. Remote sensing atmospheric water vapor using the Global Positioning System. *J. Appl. Meteorol.* 35, 830–838.
- Foster, J., Brooks, B., Cherubini, T., Shacat, C., Businger, S., Werner, C.L., 2006. Mitigating atmospheric noise for InSAR using a high resolution weather model. *Geophys. Res. Lett.* 33 (16).
- Gong, W., Meyer, F., Webley, P.W., Morton, D., Liu, S., 2010. Performance analysis of atmospheric correction in InSAR data based on the Weather Research and Forecasting Model (WRF). In: Geoscience and Remote Sensing Symposium (IGARSS), 2010. IEEE International, pp. 2900–2903.
- González, P.J., Fernandez, J., 2011. Error estimation in multitemporal InSAR deformation time series, with application to Lanzarote, Canary Islands. *J. Geophys. Res.: Solid Earth* 116 (B10).
- Guarnieri, A.M., Tebaldini, S., 2007. Hybrid Cramér–Rao bounds for crustal displacement field estimators in SAR interferometry. *IEEE Signal Process. Lett.* 14 (12), 1012–1015.
- Hanssen, R.F., Weckwerth, T.M., Zebker, H.A., Klees, R., 1999. High-resolution water vapor mapping from interferometric radar measurements. *Science* 283 (5406), 1297–1299.
- Hanssen, R.F., 2001. Radar Interferometry: Data Interpretation and Error Analysis. Kluwer Academic, Dordrecht, Boston.
- Li, Z., Muller, J.P., Cross, P., 2003. Comparison of water vapor derived from radiosonde, GPS, and Moderate-Resolution Imaging spectroradiometer measurements. *J. Geophys. Res.: Atmos.* 108 (D20).
- Li, Z.W., 2005. Modeling Atmospheric Effects on Repeat-Pass InSAR Measurements. The Hong Kong Polytechnic University, HongKong, China.
- Li, Z.W., Ding, X.L., Huang, C., Wedge, G., Zheng, D.W., 2006. Modeling of atmospheric effects on InSAR measurements by incorporating terrain elevation information. *J. Atmos. Sol. Terr. Phys.* 68 (11), 1189–1194.
- Li, Z.W., Ding, X.L., Huang, C., Zhu, J.J., Chen, Y.L., 2008. Improved filtering parameter determination for the Goldstein radar interferogram filter. *ISPRS J. Photogrammetry Remote Sens.* 63 (6), 621–634.
- Liu, S., 2012. Satellite Radar Interferometry: Estimation of Atmospheric Delay. TU Delft, Delft University of Technology.
- Massonnet, D., Rossi, M., Carmona, C., Adragna, F., Peltzer, G., Feigl, K., Rabaute, T., 1993. The displacement field of the landers earthquake mapped by radar interferometry. *Nature* 364, 138–142.
- Massonnet, D., Feigl, K.L., 1998. Radar interferometry and its application to changes in the Earth's surface. *Rev. Geophys.* 36 (4), 441–500.
- Mateus, P., Nico, G., Catalão, J., 2011. Can spaceborne SAR interferometry be used to study the temporal evolution of PWV? *Atmos. Res.* 119, 70–80.
- Mateus, P., Catalão, J., Nico, G., 2017. Sentinel-1 interferometric SAR mapping of precipitable water vapor over a country-spanning area. *IEEE Trans. Geosci. Rem. Sens.* 55 (5), 2993–2999.
- Mateus, P., Miranda, P.M., Nico, G., Catalão, J., Pinto, P., 2018. Tomé, R. Assimilating InSAR maps of water vapor to improve heavy rainfall forecasts: a case study with two successive storms. *J. Geophys. Res.: Atmos.* 123 (7), 3341–3355.
- Mengistu, T.G., Blumenstock, T., Hase, F., 2015. Observations of precipitable water vapor over complex topography of Ethiopia from ground-based GPS, FTIR, radiosonde and ERA-Interim reanalysis. *Atmos. Meas. Tech.* 8 (8), 3277–3295.
- Niell, A.E., Coster, A.J., Solheim, F.S., 2001. Comparison of measurements of atmospheric wet delay by radiosonde, water vapor radiometer, GPS, and VLBI. *J. Atmos. Ocean. Technol.* 18 (6), 830–850.
- Philippon, R., Dürr, B., Ohmura, A., Ruckstuhl, C., 2005. Anthropogenic greenhouse forcing and strong water vapor feedback increase temperature in Europe. *Geophys. Res. Lett.* 32 (19).
- Pichelli, E., Ferretti, R., Cimini, D., Panegrossi, G., Perissin, D., Pierdicca, N., Rommen, B., 2015. InSAR water vapor data assimilation into mesoscale model MM5: technique and pilot study. *IEEE J. Selected Topics in Appl. Earth Observ. Remote Sensing* 8 (8), 3859–3875.
- Puysségur, B., Michek, R., Avouac, J.P., 2007. Tropospheric phase delay in interferometric synthetic aperture radar estimated from meteorological model and multispectral imagery. *J. Geophys. Res.: Solid Earth* 112 (5).
- Rocca, F., 2007. Modeling interferogram stacks [J]. *IEEE Trans. Geosci. Rem. Sens.* 45 (10), 3289–3299.
- Samiei, Esfahany S., 2017. Exploitation of Distributed Scatterers in Synthetic Aperture Radar Interferometry. TU Delft, Delft University of Technology.
- Smith, R., 2012. Investigation of the Qadimah Fault in Western Saudi Arabia Using Satellite Radar Interferometry and Geomorphology Analysis Techniques. King Abdulla University of Science and Technology Thuwal, Kingdom of Saudi Arabia.
- Tang, W., Liao, M., Zhang, L., Li, W., Yu, W., 2016. High-spatial-resolution mapping precipitable water vapor using SAR interferograms, GPS observations and ERA-Interim reanalysis. *Atmos. Meas. Tech.* 9 (9).
- Teunissen, P., Simons, D.J., Tiberius, C., 2008. Probability and Observation Theory.
- Wadge, G., Webley, P.W., James, I.N., Bingley, R., Dodson, A., Waugh, S., Edwards, S.C., 2002. Atmospheric models, GPS and InSAR measurements of the tropospheric water vapor field over Mount Etna. *Geophys. Res. Lett.* 29 (19), 11-1.
- Wang, X.Y., Zeng, Q.M., Yun, Y., Han, K.L., Jiao, J., 2017. The reliability inspection of water vapor from WRF utilized for InSAR atmospheric correction in different areas. In: Geoscience and Remote Sensing Symposium (IGARSS), 2017. IEEE International, pp. 3105–3108.
- Yan, X., Ducrocq, V., Jaubert, G., Brousseau, P., Poli, P., Champollion, C., Flamant, C., Boniface, K., 2009. The benefit of GPS zenith delay assimilation to high-resolution quantitative precipitation forecasts: a case-study from COPS IOP 9. *Q. J. R. Meteorol. Soc.* 135 (644), 1788–1800.
- Zhang, Y., Xu, J., yang, N., Lan, P., 2018. Variability and trends in global precipitable water vapor retrieved from COSMIC radio occultation and radiosonde observations. *Atmosphere* 9 (5), 174.
- Zhao, P., Yin, Y., Xiao, H., Zhou, Y., Liu, J., 2016. Role of water vapor content in the effects of aerosol on the electrification of thunderstorms: a numerical study. *Atmosphere* 7 (10), 137.